Computers and Geotechnics 123 (2020) 103566

Contents lists available at ScienceDirect

Computers and Geotechnics

journal homepage: www.elsevier.com/locate/compgeo

Research Paper

Responses of geosynthetic-reinforced soil (GRS) abutments under bridge slab loading: Numerical investigation

Panpan Shen[a], Jie Han[b,*], Jorge G. Zornberg[c], Burak F. Tanyu[d], Barry R. Christopher[e], Dov Leshchinsky[f]

[a] Department of Geotechnical Engineering, School of Civil Engineering, Tongji University, Shanghai 200092, China
[b] The University of Kansas, CEAE Department, Lawrence, KS 66044, USA
[c] The University of Texas at Austin, Civil Engineering Department, Austin, TX 78712, USA
[d] Department of CEIE, George Mason University, Fairfax, VA 22030, USA
[e] Geotechnical Consultant, 210 Boxelder Lane, Roswell, GA 30076, USA
[f] ADAMA Engineering, Inc., Clackamas, OR 97015, USA

ARTICLE INFO

Keywords:
Bridge abutment
Geosynthetic
Geosynthetic-reinforced soil
Numerical
Surcharge

ABSTRACT

This study evaluated the responses of geosynthetic-reinforced soil (GRS) abutments subjected to bridge slab loading under working stress conditions using two-dimensional finite difference numerical software. A parametric study was conducted to investigate the effects of different combinations of reinforcement spacing S_v and reinforcement stiffness J, beam seat width b, and setback distance a_b on the responses of the GRS abutments in terms of additional vertical stresses under the beam seat centerline $\Delta\sigma_v$ induced by the bridge slab load, additional lateral earth pressures behind the abutment facing $\Delta\sigma_{h\text{-}facing}$ and under the beam seat centerline $\Delta\sigma_{h\text{-}cetner}$ induced by the bridge slab load, and maximum tension in the reinforcement T_{max}. Numerical analyses evaluated trapezoidal and uniform reinforcement layouts and showed that both reinforcement layouts generated similar responses of the GRS abutments. Under the same ratio of J/S_v, different combinations of S_v and J generated similar distributions of $\Delta\sigma_v$, $\Delta\sigma_{h\text{-}facing}$ and $\Delta\sigma_{h\text{-}center}$. The maximum of T_{max} with depth decreased almost proportionally with the decrease of S_v. Larger b and a_b caused lower $\Delta\sigma_v$, $\Delta\sigma_{h\text{-}facing}$, $\Delta\sigma_{h\text{-}center}$, and smaller T_{max} in the upper reinforcement layers. The truncated 2 to 1 distribution method, which considers the effects of abutment facing on the $\Delta\sigma_v$ distribution, could reasonably predict the T_{max} in the reinforcement.

1. Introduction

Geosynthetics have been successfully employed as reinforcement elements to reinforce backfill soil in geosynthetic-reinforced retainting structures, which are often under surcharge-free conditions. Previous experimental and theoretical studies have investigated the behavior of geosynthetic-reinforced retaining structures under both serviceability and strength limit states. The American Association of State Highway and Transportation Officials (AASHTO) recommended a tied-back wedge method for internal stability analysis and a gravity wall method for external stability analysis of the Mechanically Stabilized Earth (MSE) Walls[1]. Allen et al. [6] and Bathurst et al. [10] proposed the K-stiffness method to predict the maximum tension in the reinforcement based on field data obtained from a variety of geosynthetic-reinforced retaining walls, which were normally under serviceability limit states. Han and Leshchinsky [17], Leshchinsky et al. [22], and Leshchinsky et al. [23] proposed a limit equilibrium (LE) design framework for geosynthetic-reinforced earth structures including both walls and slopes. This framework utilized an iterative top-down procedure for LE analysis of slope stability to determine the distribution of required reinforcement tnsile strengths to attain a prescribed LE state.

More recently, geosynthetic-reinforced retaining structures have been increasingly used as bridge abutments to support surcharge loads. These types of structures are frequently referred to in the literature as geosynthetic-reinforced soil (GRS) structures. The surcharge loads on GRS abutments are often large and close to the abutment facing [19]. Several field projects reported in the literature (e.g., [2,29]; and [28]) showed satisfactory performance with regard to lateral facing displacements and post-construction settlements of the bridge sill. The US Federal Highway Administration (FHWA) recommended the use of a

* Corresponding author.
E-mail addresses: 18310183@tongji.edu.cn (P. Shen), jiehan@ku.edu (J. Han), zornberg@mail.utexas (J.G. Zornberg), btanyu@gmu.edu (B.F. Tanyu), barryc325@aol.com (B.R. Christopher), adama@GeoPrograms.com (D. Leshchinsky).

https://doi.org/10.1016/j.compgeo.2020.103566
Received 1 February 2020; Received in revised form 20 March 2020; Accepted 28 March 2020
Available online 10 April 2020

GRS performance test (also referred to as the GRS mini-pier test) to evaluate the vertical load-deformation behavior of a GRS mass with frictionally-connected facing units [4]. A small number of GRS mini-pier tests have been reported in the literature to determine the ultimate bearing capacities and the stress–strain relationships of the GRS masses [15,3,27,26,34]. However, the boundary conditions of the GRS mini-pier tests are different from those of the GRS abutments constructed in the field. The GRS mini-pier tests simulated a three-dimensional (3D) stress state (close or similar to a triaxial condition) while the GRS abutments had a two-dimensional (2D) plane strain condition [31]. Therefore, the results of the GRS mini-pier tests may not accurately represent the GRS abutments in the field.

As compared to investigations of geosynthetic-reinforced retaining structures without any surcharge, fewer studies have been carried out to evaluate the behavior of the GRS abutments under surcharge loads. Xiao et al. [30] and Xie et al. [32] investigated the ultimate bearing capacities and failure modes of strip footings on top of GRS walls experimentally and theoretically. Ahmadi and Bezuijen [5] utilized two full-scale model tests to investigate the wall facing displacements and the reinforcement tension distributions in GRS walls subjected to strip footing loading under a serviceability limit state and proposed corresponding theoretical solutions. Other researchers have conducted numerical studies on the serviceability-state behavior of GRS walls and abutments under footing loads, including lateral facing displacements and footing settlements [7,33,35–38]. Limited studies have focused on the responses of the GRS abutments under bridge slab loading considering different influencing factors and reinforcement layouts, including the additional vertical stresses and additional lateral earth pressures. Understanding of these additional vertical stresses and lateral earth pressures is crucial to determine the required strength of geosynthetic reinforcement. The FHWA design guidelines for MSE walls [11] recommended a 2 (vertical) to 1 (horizontal) distribution to estimate the vertical and horizontal stresses induced by the footing load based on instrumented data and numerical modeling. This distribution was later adopted in the AASHTO recommendation [1]. However, the influence of different reinforcement layouts (e.g., reinforcement spacing) has not been evaluated for the 2 to 1 distribution as compared to the Boussinesq distribution recommended by the FHWA for geosynthetic-reinforced soil – integrated bridge system (GRS-IBS) [4].

In this study, two-dimensional finite difference numerical investigations were carried out to evaluate the responses of GRS abutments subjected to bridge slab loading under working stress conditions. The numerical model was first validated by a field monitored GRS-IBS constructed in Virginia, USA. A parametric study was then conducted to investigate the effects of the following influencing factors, including different combinations of reinforcement spacing S_v and reinforcement stiffness J, beam seat width b, and setback distance a_b, on the responses of the GRS abutments in terms of the additional vertical stresses and lateral earth pressures induced by the bridge slab load and the maximum tension T_{max} in the reinforcement. This study also considered the effects of two different reinforcement layouts (trapezoidal and uniform) on the behavior of the GRS abutments. These two different reinforcement layouts were selected based on the recommendations from two different design guidelines.

2. Overview of the Virginia GRS-IBS

A field monitored GRS-IBS constructed in Virginia [40,16] was chosen for numerical modeling carried out in this study. The Virginia GRS-IBS was of interest since it was approximately the same height as the GRS mini-piers conducted by the FHWA [26], thus allowing a direct comparison of the performance of the field GRS-IBS and the GRS mini-pier at working stress conditions. The cross section of Abutment A of the Virginia GRS-IBS was simulated in the numerical model as shown in Fig. 1. The Virginia GRS-IBS is composed of a reinforced soil foundation (RSF), a reinforced zone, 11 layers of Concrete Masonry Unit (CMU) facing blocks, a geofoam, a bridge slab, and an integrated approach. The geometry of the numerical model was based on the actual dimensions of the Virginia GRS-IBS constructed in the field, with some minor modifications to simplify the numerical mesh. The RSF, constructed using the Virginia Department of Transportation (VDOT) 21B aggregate (hereinafter referred to as VDOT21B), had a thickness D_f of 0.7 m and a length B_f of 3.5 m. Woven geotextiles were used as reinforcement to form the wrapped-around RSF with an additional reinforcement layer in the middle. The RSF was seated on limestone bedrock and surrounded by the foundation soil. The abutment itself had a height H of 2.4 m (including the beam seat behind the geofoam) with three vertical cut slopes at back. As previously noted, this height was similar to that of the GRS mini-piers. The base length B_a was 2.6 m and the total base length B_{total}, including the CMU facing blocks, was 2.8 m. The AASHTO No. 8 aggregate (hereinafter referred to as AASHTO No. 8) was used as the backfill soil for the reinforced zone. The same type of woven geotextiles was used as the reinforcement in the reinforced zone, with a vertical spacing S_v of 0.2 m between primary reinforcement layers. The primary reinforcement layers in the reinforced zone extended to the cut slopes with three different lengths as shown in Fig. 1. Five layers of bearing reinforcement layers (or secondary reinforcement) were used in the reinforced zone. The length of the bearing reinforcement L_{rb} was 1.6 m. The vertical spacing of the bearing reinforcement layers was half of the spacing between the primary reinforcement layers (i.e., S_{vb} = 0.1 m). Solid CMU blocks were used for the first four layers and hollow CMU blocks were used for the remaining seven layers to construct the abutment facing. All the CMU facing blocks had dimensions of 0.2 m wide × 0.2 m high. The geofoam was located on top of the CMU facing blocks and had dimensions of 0.4 m wide × 0.2 m high. The clear spacing d_e, defined as the distance from the top of the uppermost CMU facing block to the bottom of the bridge slab, was the same as the height of the geofoam (i.e., d_e = 0.2 m). The beam seat width b was 0.6 m and the setback distance a_b for the beam seat was 0.2 m. The bridge slab had a length L_b of 5.6 m and a thickness D of 0.4 m. The integrated approach, constructed with the VDOT21B, had two lifts of wrapped-around fill material behind the bridge slab. The same type of woven geotextiles was used as the reinforcement in the integrated approach.

3. Numerical Modeling

The finite difference method-based program FLAC2D (Fast Lagrangian Analysis of Continua) was used to simulate the Virginia GRS-IBS. Fig. 1 shows the numerical model mesh. To minimize the influence of boundary conditions, the foundation soil was 2.4 m deep (1H) and the left lateral boundary was located at 8.5 m (3.5H) behind the abutment facing. The right lateral boundary was located at 1.5 m in front of the abutment facing based on the symmetry of the bridge slab. Lateral boundaries were fixed in the horizontal direction and were free to move in the vertical direction, while the bottom boundary was fixed in both horizontal and vertical directions.

3.1. Constitutive models

The backfill soil AASHTO No. 8 used in the reinforced zone was classified as a poorly graded gravel (GP) according to the Unified Soil Classification System (USCS) with no fines and was modeled using the Cap-Yield (CY) model based on the theory of hardening plasticity [21]. The CY model is a double yield model, which considers both isotropic compression yielding and shear yielding. The CY model provides a better representation of the nonlinear behavior of soils and allows a more realistic representation of the loading/unloading response of soils [21]. In the CY model, the reference pressure p_{ref} was set as 34.5 kPa, which was the same as one of the confining stresses used in the triaxial compression tests. The typical failure ratio R_f of 0.9 was used. The CY surface was assumed to be spherical and therefore the CY surface

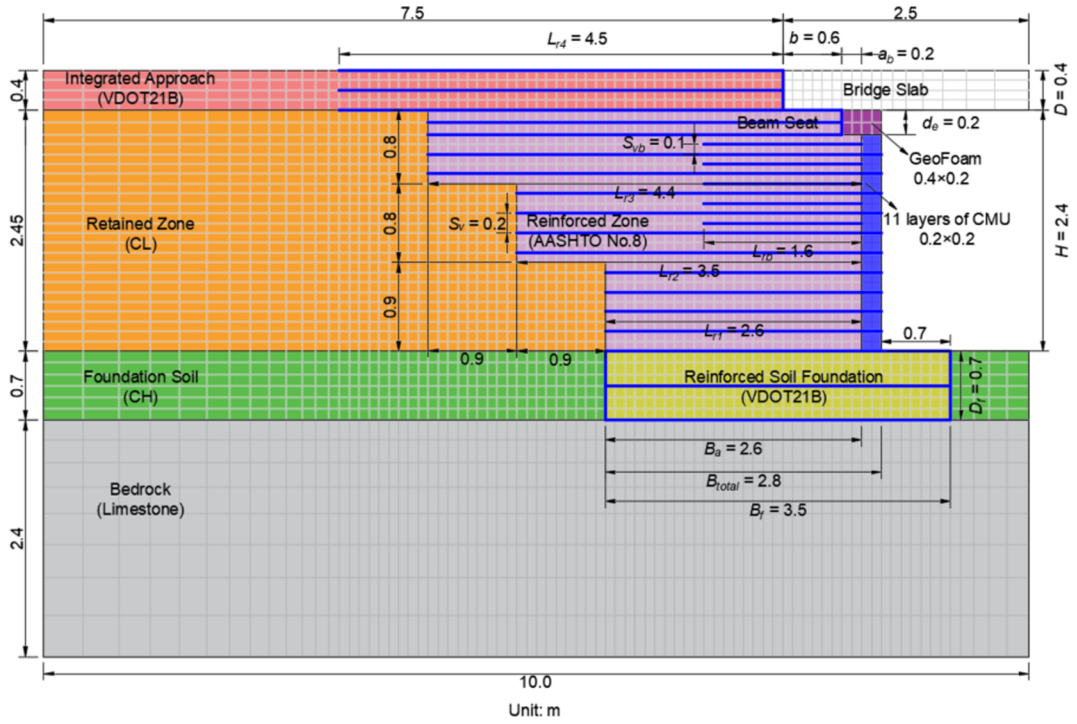

Fig. 1. Cross-section and numerical model mesh for the Virginia GRS-IBS (unit: m).

Table 1
Parameters of AASHTO No. 8 backfill soil for the CY model.

Parameters	Unit	Value
Density	kg/m^3	1650
Cap-Yield surface parameter α	/	1.0
Friction angle	∘	50
Dilation angle	∘	20
Cohesion	kPa	0
Multiplier R	/	5.9
Plastic strain coefficient β	/	0.15
Reference tangent shear modulus G^e_{ref}	MPa	36.2
Reference bulk modulus K^{iso}_{ref}	MPa	7.0
Power m	/	0.55
Reference pressure p_{ref}	kPa	34.5
Poisson's ratio	/	0.2
Failure ratio	/	0.9

parameter α was set as 1. The reference tangent shear modulus G^e_{ref} and the plastic strain coefficient β were calibrated from the deviatoric stress versus axial strain curves from the triaxial compression test results. Due to lack of reliable oedometer loading test data or isotropic compression test data, the bulk modulus at the reference pressure K^{iso}_{ref} and the power m were derived as a result of calibration using the volumetric strain versus axial strain curves from the triaxial compression tests. Table 1 summarizes the parameters used in the CY model. Fig. 2 shows a comparison between the results from the triaxial compressive tests and the numerical simulations, in which the stress-dependent CY model can capture the nonlinear stress - strain behavior of the soil prior to failure.

Table 2 lists all the constitutive models and input parameters for the rest components simulated in the numerical model apart from the AASHTO No. 8. The friction angle ϕ and the cohesion c of the VDOT21B were chosen based on the results of direct shear tests. The relationship recommended by Bolton [12] (i.e., $\psi = \phi - 30°$) was used to determine a dilation angle ψ. The retained soil and the foundation soil were classified as CL and CH respectively according to the USCS soil

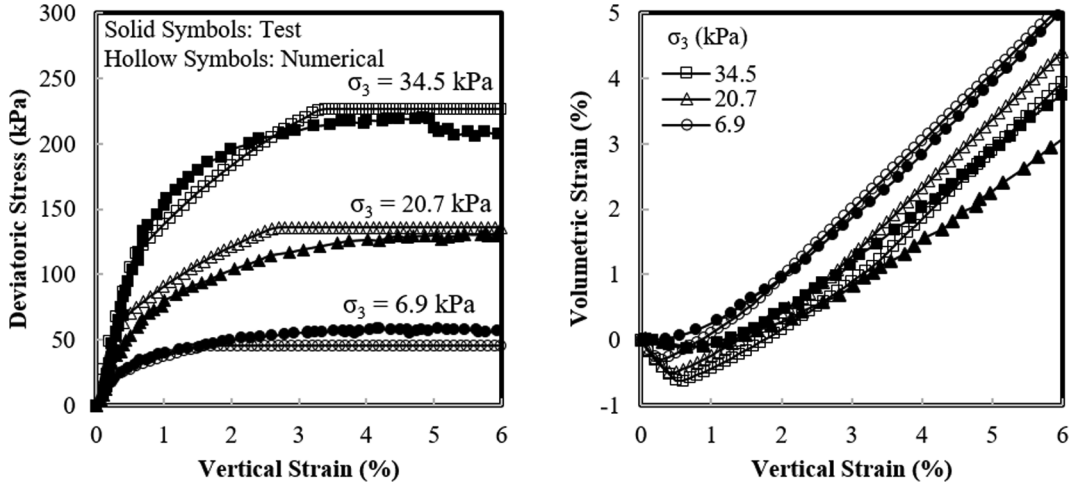

Fig. 2. Comparison between the measured and simulated triaxial compression test results.

Table 2
Constitutive models and input parameters for different components simulated in the numerical model apart from AASHTO No. 8.

Components	Constitutive models	Input parameters
VDOT21B	Mohr-Coulomb	ρ = 2200 kg/m^3, E = 25 MPa, υ = 0.2,ϕ = 48.3°, c = 5.6 kPa, ψ = 18.3°
Retained soil (CL)	Mohr-Coulomb	ρ = 1750 kg/m^3, E = 20 MPa, υ = 0.3,ϕ = 30°, c = 20 kPa
Foundation soil (CH)	Mohr-Coulomb	ρ = 1750 kg/m^3, E = 20 MPa, υ = 0.3,ϕ = 26°, c = 20 kPa
Limestone bedrock	Linear-elastic	ρ = 2000 kg/m^3, E = 2 GPa, υ = 0.2
Bridge slab	Linear-elastic	ρ = 2500 kg/m^3, E = 20 GPa, υ = 0.2
CMU blocks	Linear-elastic	ρ = 1800 and 1250 kg/m^3 for solid and hollow CMU blocks respectively, E = 20 GPa, υ = 0.2
Geofoam	Linear-elastic	ρ = 11.2 kg/m^3, E = 1.5 MPa, υ = 0.15

Note: ρ – density; E - Elastic modulus; υ - Poisson's ratio; ϕ - friction angle; c - cohesion; ψ - dilation angle.

classification. The measured liquid limit (LL) and plasticity limit (PL) for the retained soil were 42 and 19 respectively, resulting in a plasticity index (PI) of 23. The measured LL and PL for the foundation soil were 50 and 23 respectively, resulting in a PI of 27. The elastic moduli E, Poisson's ratio υ, the densities ρ, and the cohesion c of the retained soil and the foundation soil were chosen based on the typical values recommended by Coduto [13]. The correlation recommended by Mitchell and Soga [24] (i.e., $\sin\phi \approx 0.8–0.094 \ln PI$) was used to determine the friction angles ϕ of the retained soil and the foundation soil. Solid CMU blocks were used for the first four layers and hollow CMU blocks were used for the remaining seven layers to construct the abutment facing. The properties of the geofoam were provided by the manufacturer.

3.2. Geotextile reinforcement and interfaces

A woven geotextile was used as the reinforcement in the Virginia GRS-IBS. The wide-width tensile strengths of the geotextile were 14 and 70 kN/m at 2% and 10% strains respectively in the machine direction (MD), which were confirmed by the wide-width tensile tests performed as part of the National Cooperative Highway Research Program (NCHRP) study [40]. Therefore, the tensile stiffness J of the geotextile at both strain levels was 700 kN/m. Both cable structural elements and beam structural elements embedded in FLAC2D were used in the numerical model to simulate the geotextile reinforcement layers. Beam structural elements with zero moment of inertia (i.e., no bending stiffness) and frictional interfaces on both sides were used to simulate the horizontal geotextile layers between the CMU facing blocks, the horizontal geotextile layers between the CMU facing blocks and the RSF, the vertical geotextile layers between the beam seat and the geofoam, and the vertical geotextile layers between the integrated approach and the bridge slab. Cable structural elements with embedded frictional interfaces on both sides were used to simulate the remaining geotextile layers within the backfill soil. Fig. 3 shows different structural elements and their interface details used in the numerical model. The properties of both the beam and cable structural elements were determined based on the actual properties of the woven geotextiles used in the construction of the Virginia GRS-IBS. Assuming the thickness t of the geotextile was 1 mm, the elastic modulus of the structural elements was calculated as 700 MPa by dividing their tensile stiffness by the thickness.

Different types of interfaces were used in the numerical model, as shown in Table 3. These interfaces were represented by interface elements included in the software, which are linearly-elastic perfectly-plastic springs with an MC failure criterion. The properties of the CMU-geotextile (frictional) interface were chosen based on pullout test results of Awad and Tanyu [9]. An interface cohesion of 9.5 kPa was justified because some irregularities existing on the rough surfaces of concrete could behave like cohesion by preventing the geotextile from moving. The top three layers of CMU facing blocks were connected using dowel bars in the field. In the numerical model, the dowel bars were simulated as mechanical connections using the properties recommended by Huang et al. [20]. The bearing reinforcement layers were not connected to the CMU facing blocks. For the interfaces related to the geofoam, a friction coefficient of 0.5 (i.e., interface friction angle δ = arctan(0.5) = 26.6°) and zero cohesion were used [25].

3.3. Modeling procedure

Field construction of the Virginia GRS-IBS took place in stages, which were simulated in the numerical modeling conducted in this study. The construction stages adopted in the simulations were as follows:

Stage 1: Prior to the abutment construction, the limestone bedrock and the foundation soil reached an equilibrium under gravity.

Stage 2: The construction of the RSF was simulated and the

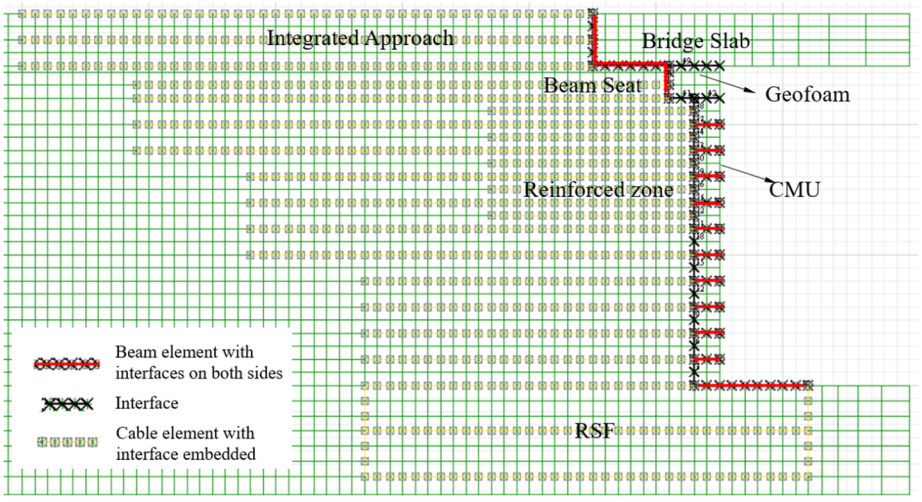

Fig. 3. Geotextile reinforcement and interface details.

Table 3
Interface properties used in the numerical model of the Virginia GRS-IBS.

Interface	Method	C_i	δ (°)	c_{in} (kPa)
Geotextile-VDOT21B	Embedded in cable element	0.9	45.3	0
Geotextile-AASHTO No.8	Embedded in cable element	0.9	47.0	0
CMU-AASHTO NO.8	Interfaces	0.65	37.8	0
CMU-Geotextile (Frictional)	Beam elements with interfaces	/	16.2[a]	9.5[a]
CMU-Geotextile (Mechanical)	Beam elements with interfaces	/	57.0[b]	46[b]
Geofoam-Geotextile, Geofoam-CMU, andGeofoam-Bridge slab	Interfaces	/	26.6[c]	0
Bridge slab-Geotextile	Beam elements with interfaces	/	16.2[a]	9.5[a]

Note: C_i - interaction coefficient; δ - interface friction angle; c_{in} - interface cohesion; [a]Based on Awad and Tanyu [9],[b]Based on Huang et al. [20],[c]Based on Negussey [25].

geotextiles were placed in the RSF.

Stage 3: A layer of the CMU facing block, the backfill soil (AASHTO No. 8), the retained soil, and the geotextile were installed. Corresponding interfaces and connections were assigned. The abutment was under a self-weight condition after this construction stage was finished.

Stage 4: The geofoam and the beam seat were installed. Corresponding interfaces and connections were assigned

Stage 5: After the construction of the abutment was finished, the bridge slab was placed on top of the beam seat. Corresponding interfaces and connections were assigned.

Stage 6: The integrated approach was constructed behind the bridge slab. Geotextiles were installed in the integrated approach.

Compaction was simulated during the construction of the numerical model of the Virginia GRS-IBS. A uniform vertical stress of 8 kPa as used by Hatami and Bathurst [18] and Zheng and Fox [36] was applied on top of each lift of the backfill soil layer and removed before the placement of next lift to simulate the compaction effect in the field.

3.4. Stage loading

Seven stage loadings (SL) using single or multiple Jersey barriers at different elevations were performed during the construction of the Virginia GRS-IBS to evaluate the influence of different reinforcement spacing used in the abutment (i.e., 0.1 and 0.2 m) on the vertical stress distributions beneath rigid footings under surcharge loads. Detailed information about the SL can be found in Zornberg et al. [40] and Gebremariam et al. [16]. Among seven SLs, SL1, SL3, and SL5 were applied using a single Jersey barrier as the surcharge load, while the remaining four SLs used eight Jersey barriers. Four SLs were applied on the reinforcement zone with reinforcement spacing S_v of 0.2 m (i.e., SL1 to SL4) and three SLs were applied on the reinforced zone with bearing reinforcement of S_{vb} = 0.1 m (i.e., SL5 to SL7). The load from a single Jersey barrier was approximately 24 kN. The bottom of a single Jersey barrier was 3.7 m long and 0.6 m wide. As a result, the average equivalent vertical stress from a single Jersey barrier was approximately 11 kPa. Fig. 4 shows the schematic of SL3 and SL7. The small notch at the bottom of the Jersey barrier resulted in a non-uniform stress distribution when eight Jersey barriers were applied, as shown in Fig. 4(b). The load from seven Jersey barriers was applied to the bottom left and right Jersey barriers with an average equivalent vertical stress of approximately 38.5 kPa on each end, resulting in an average equivalent vertical stress of 11 kPa from the middle Jersey barrier.

These seven SLs were also simulated in numerical modelling during Stage 3. The Jersey barriers used in the field were similar to rigid footings. Simulating stage loading with a uniform vertical stress was deemed not appropriate because the contact pressure at the bottom of the Jersey barrier was not uniform. Instead of a uniform vertical stress, the numerical model used rectangular blocks of 0.6 m wide and 0.1 m high to simulate the load. Since the Jersey barriers were made of concrete, a typical elastic modulus of 20 GPa and Poisson's ratio of 0.15 were assigned to these rectangular blocks. Different densities were assigned to these rectangular blocks as shown in Fig. 5 in order to simulate the non-uniform stress distribution when eight Jersey barriers were used. For the SLs using a single Jersey barrier (i.e., SL1, SL3, and SL5), the rectangular block had a density of 11225 kg/m^3 as shown in Fig. 5(a), resulting in an average vertical stress of 11 kPa at the bottom of the block. For the SLs using multiple Jersey barriers (i.e., SL2, SL4, SL6, and SL7), the bottom three rectangular blocks had the same density of 11225 kg/m^3 while the top two blocks had a density of 28061 kg/m^3 as shown in Fig. 5(b), resulting in an average vertical stress of 38.5 kPa at the bottom of the left and right blocks.

3.5. Numerical model validation

The numerical model was validated using field instrumentation results of the Virginia GRS-IBS. Detailed information of the field instrumentation can be found in Zornberg et al. [40] and Gebremariam et al. [16]. Fig. 6(a) shows a comparison between the numerically simulated and the measured lateral earth pressures behind the abutment facing under the self-weight (i.e., end of Stage 3). The measured lateral earth pressures, which were obtained using rectangular contact pressure cells, were close to the numerical results. Fig. 6(a) also shows the lateral earth pressure profiles calculated using the Rankine active earth pressure coefficient K_a and the lateral earth pressure coefficient at-rest K_o at the end of Stage 3 (i.e., under self-weight condition). Because of the SLs, the lateral earth pressure behind the abutment facing did not show a proportional increase with depth. The numerically simulated lateral earth pressures were similar to the at-rest lateral earth pressure (K_o condition) for the upper portion of the abutment where the bearing reinforcement layers existed and the reinforcement spacing S_{vb} was 0.1 m. For the lower portion of the abutment where the reinforcement spacing S_v was 0.2 m, the numerical analyses using the CY model showed the effect of the SLs. The lateral earth pressure increased at the elevation where the SLs using multiple Jersey barriers were applied. Since the CY model is stress-dependent, stage loading and unloading led to an increase in the soil modulus. Consequently, the lateral displacement of the CMU facing blocks decreased and the lateral earth pressure behind the abutment facing increased. Fig. 6(b) shows the additional lateral earth pressures behind the abutment facing induced by the bridge slab load. The additional lateral earth pressure refers to the lateral earth pressure induced by the bridge slab load only. In other words, the reference "zero" lateral earth pressure was set at the end of Stage 4 (i.e., after the installation of the geofoam and the beam seat). Fig. 6(b) indicates that the numerical results matched reasonably well with the field data. Higher additional lateral earth pressures were induced near the top portion of the abutment. The SLs resulted in a non-smooth distribution of the additional lateral earth pressures with depth.

Fig. 7 shows a comparison of the additional vertical stresses induced by the bridge slab load measured in the field, the results from the numerical simulation, and the theoretical stress calculations using the Boussinesq solution recommended by the FHWA for GRS-IBS [4], and the truncated 2 to 1 distribution recommended by both the FHWA for MSE walls [11] and the AASHTO [1]. Similar to the additional lateral

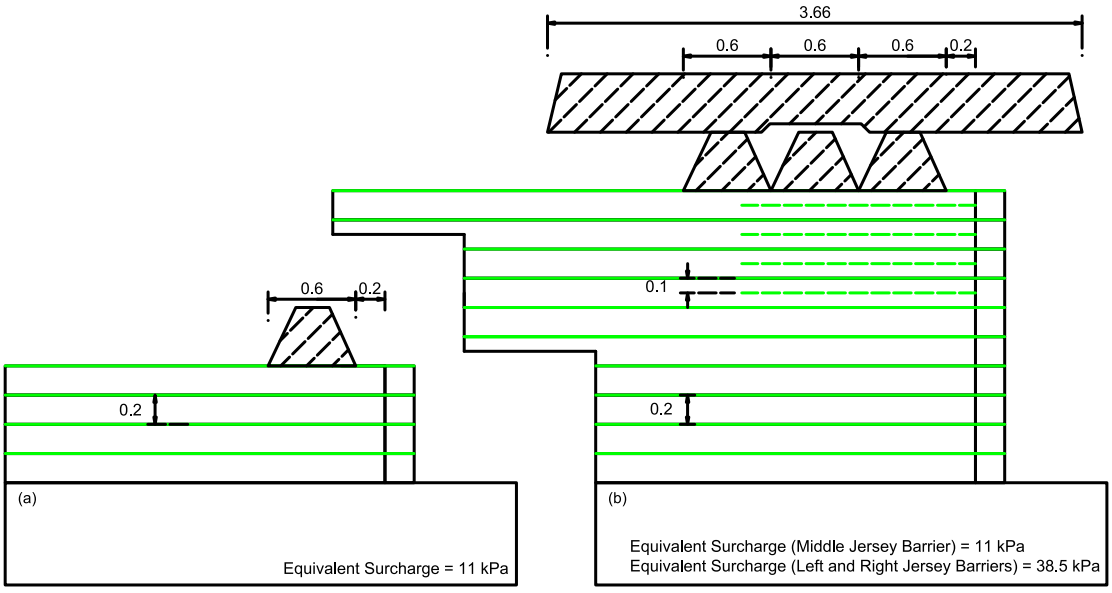

Fig. 4. Schematic of stage loading (unit: m): (a) SL3; and (b) SL7.

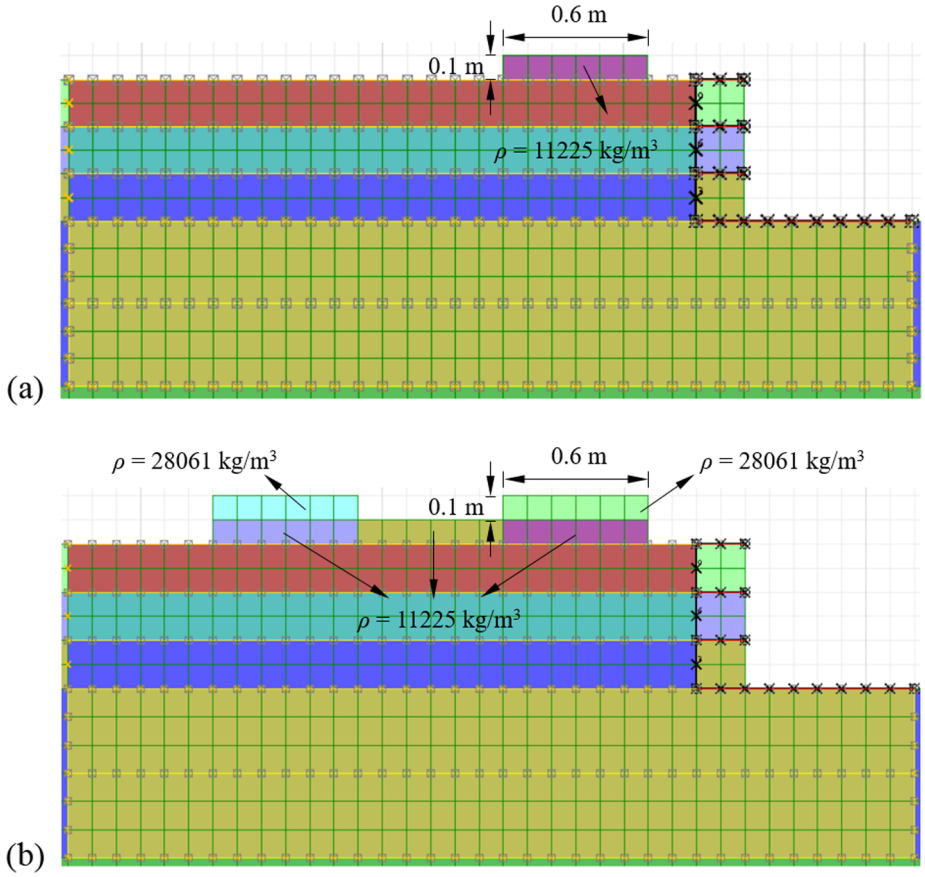

Fig. 5. Numerical simulation of SL: (a) single Jersey barrier; and (b) multiple Jersey barriers.

earth pressure discussed previously, the additional vertical stress refers to the vertical stress induced by the bridge slab load only. Fig. 7 also shows that the numerical results matched reasonably well with the field data. Furthermore, the magnitudes of the stresses obtained from the field and the numerical analyses are comparable with those predicted by the theoretical calculations. The additional vertical stresses induced by the bridge slab load were higher at the top and decreased with depth. Additionally, the numerical results show the effects of the SLs as a non-smooth distribution of the additional vertical stresses with depth.

Fig. 8 shows the distributions of the measured and numerically simulated geotextile strains with depth. The strain gauges were located 0.3 m away from the back of CMU facing blocks in the field. Fig. 8 presents two construction stages, which were under self-weight (i.e., Stage 3) and bridge slab loading (i.e., Stage 5). Fig. 8 shows that the numerical results were in good agreement with the measured data, although the measured strains were slightly larger than those

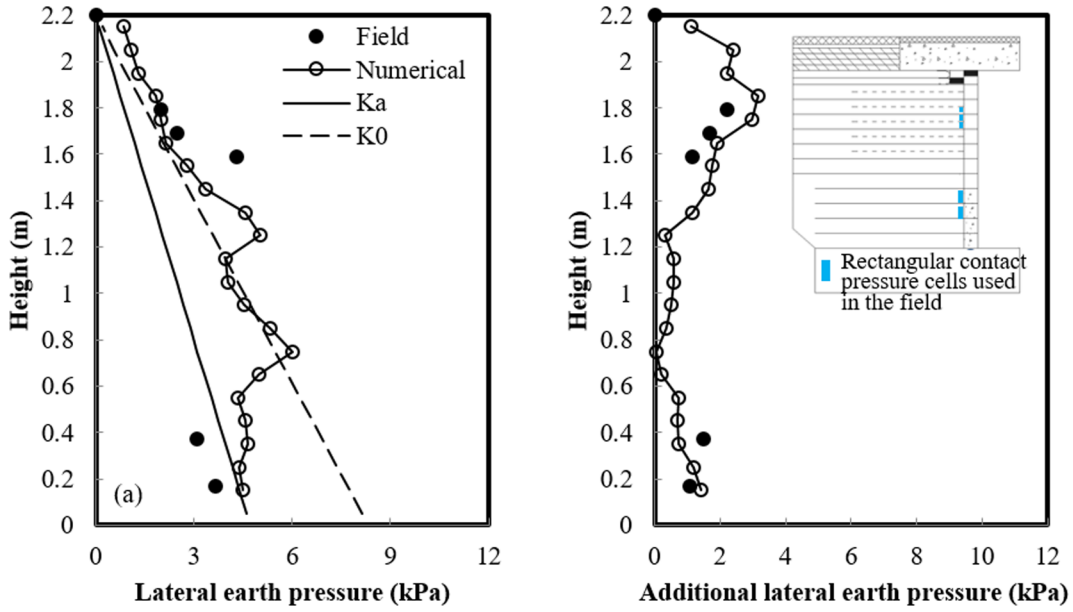

Fig. 6. Lateral earth pressures behind the abutment facing: (a) under self-weight; and (b) induced by the bridge slab load.

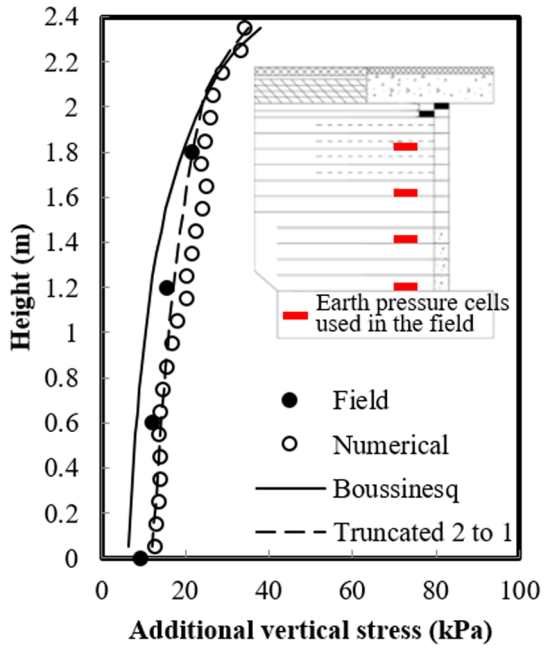

Fig. 7. Additional vertical stresses 0.3 m away from the back of CMU facing blocks induced by the bridge slab load.

numerically simulated under the self-weight condition. Numerical results also show that larger strains developed in the primary reinforcement (as shown in Fig. 8 with triangular symbols) and smaller strains developed in the bearing reinforcement layers (as shown in Fig. 8 with circular symbols) because the bearing reinforcement layers were not connected with the CMU facing blocks.

Overall, the numerical model developed in this study was able to reasonably simulate the field performance of the Virginia GRS-IBS in terms of the lateral earth pressures, the additional vertical stresses, and the reinforcement strains. Therefore, a parametric study was conducted using the numerical model developed in this section.

4. Parametric Study

4.1. Numerical models considering two different reinforcement layouts

The Virginia GRS-IBS had a layout recommended by Adams and Nicks [4] with shorter reinforcement layers at the bottom and longer reinforcement layers at the top (hereinafter referred to as the trapezoidal layout). However, uniform reinforcement length throughout the whole height is commonly used in practice when MSE walls are utilized as bridge abutments (hereinafter referred to as the uniform layout). In the parametric study, two geometries considering different reinforcement layouts were selected for a comparison. Fig. 9 shows the geometries of both the trapezoidal and the uniform layouts.

The trapezoidal layout involved a 1:1 cut slope of the retained soil, while the uniform layout consisted of a vertical cut slope of the retained soil. A 6-m high abutment (H = 6 m) was selected as typical for MSE walls used in practice. To minimize the influence of the boundary conditions, the depth of the foundation soil was 7.5 m (approximately 1.25H) and the left lateral boundary was located at 21 m (3.5H) behind the abutment facing. The bridge slab had a length L_b of 15 m and a thickness D of 0.4 m. The right lateral boundary was selected based on the symmetry of the bridge slab (i.e., at $1/2L_b$). Lateral boundaries were fixed in the horizontal direction but free to move in the vertical direction, while the bottom boundary was fixed in both horizontal and vertical directions.

The trapezoidal layout had a RSF thickness D_f of 0.7 m, resulting in a free abutment height of 5.3 m. To maintain the same free abutment height for both layouts, a 0.7 m thick embedment was assigned to the uniform layout in front of the abutment facing. The lengths of all reinforcement layers were such that they reached the cut slope. The reinforcement length for the trapezoidal layout increased proportionally from the bottom of the abutment to the top along the 1:1 cut slope. The reinforcement length at the bottom of the abutment for the trapezoidal layout was 2.6 m, as shown in Fig. 9(a). Assuming the reinforcement extended to the bottom of the RSF along the same 1:1 cut slope, the reinforcement length at the bottom of the RSF was 1.9 m. The reinforcement length at the top of the wall for the trapezoidal layout was 7.8 m. Therefore, the average length of the reinforcement for the trapezoidal layout was 4.9 m. To facilitate an equivalent comparison, the uniform reinforcement length in the uniform layout was also set as 4.9 m, as shown in Fig. 9(b). It should be noted that this length is

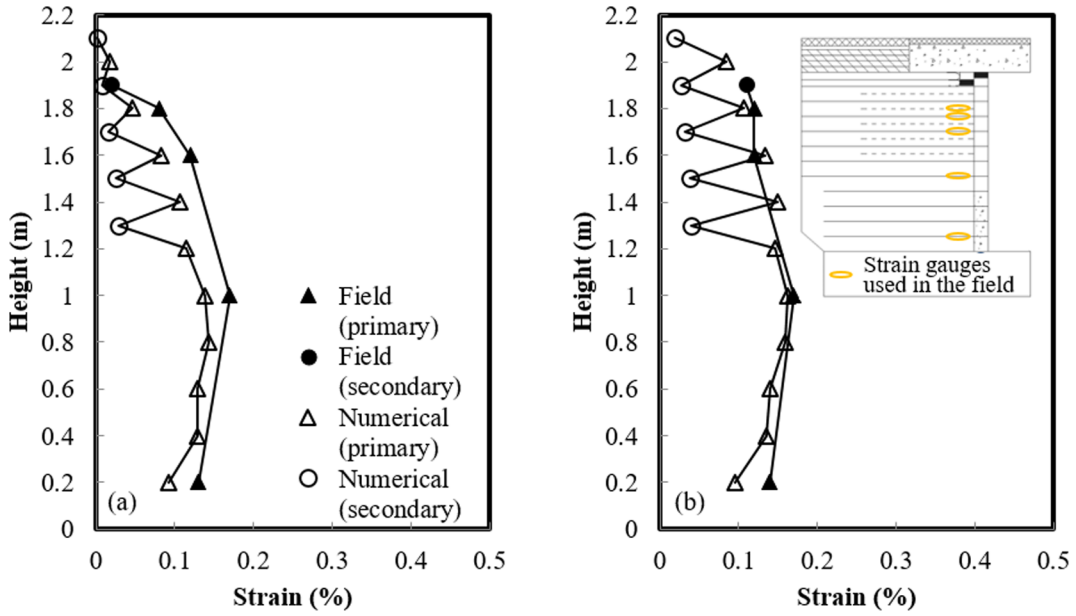

Fig. 8. Geotextile strain distributions with depth under: (a) self-weight and (b) bridge slab loading.

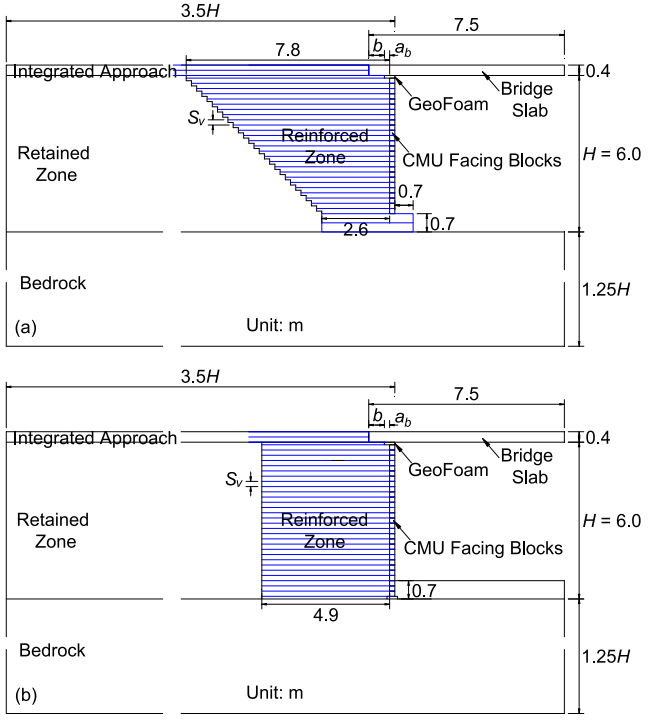

Fig. 9. Geometries of numerical models considering different reinforcement layouts: (a) trapezoidal layout and (b) uniform layout.

consistent with the minimum reinforcement length of 0.7H required in the FHWA guidelines for MSE walls [11]. No bearing reinforcement was used in the parametric study.

Table 4 lists all the variables considered in the parametric study. The primary objective of this parametric study was to investigate the effects of different combinations of reinforcement spacing S_v and reinforcement stiffness J, beam seat width b, setback distance a_b, and different reinforcement layouts (i.e., trapezoidal and uniform) on the responses of the GRS abutments in terms of additional vertical stress and lateral earth pressure induced by the bridge slab load and the maximum tension in the reinforcement. Three different combinations of reinforcement spacing S_v and reinforcement stiffness J were adopted in the parametric study while the ratio of reinforcement stiffness to spacing was maintained the same as J/S_v = 3500 kN/m/m. The beam seat width and the setback distance were two factors related to the bridge slab load. That is, the beam seat width was related to the dimension of the loading area and the setback distance was related to the position of the load. Therefore, these two factors would change the stress distribution within the reinforced zone, thus resulting in different responses of the GRS abutments subjected to the bridge slab load under working stress conditions. All analyses were run under both reinforcement layouts.

The constitutive models and the parameters of the retained soil, the bedrock, the bridge slab, the CMU facing blocks, and the geofoam were the same as those used in the Virginia GRS-IBS as described in Section 3. However, a cohesionless soil with a friction angle of 38° was selected for the backfill soil in the reinforced zone and the integrated approach considering the recommendation from Adams and Nicks [4] that the friction angle of the backfill soil used in the design of GRS abutments should not be less than 38°. A dilation angle of 8° was selected following the relationship recommended by Bolton [12]. Other parameters of the backfill soil were identical to those used in the Virginia GRS-IBS.

The structural elements used to simulate the geotextile reinforcement layers were kept as the same as those used in the Virginia GRS-IBS. Interface properties were also kept as the same except for some

Table 4
Variables considered in the parametric study.

Variable	Symbol (unit)	Value
Combinations of reinforcement spacing and reinforcement stiffness	J/S_v (kN/m/m)	700/0.2, 1400/0.4, and 2100/0.6
Beam seat width	b (m)	0.6, 0.9, and 1.2
Setback distance	a_b (m)	0.2, 0.4, and 0.8
Reinforcement layout	/	Trapezoidal and uniform

Table 5
Interface properties used in the parametric study.

Interface	C_i	δ (°)	c_{in} (kPa)
Geotextile-Backfill soil	0.9	35.1	0
CMU-Backfill soil	0.65	26.9	0
CMU-Embedment soil		20.6	0
CMU-Geotextile (Frictional)	/	16.2	9.5
CMU-CMU	/	31.0	0
Geofoam-Geotextile & Geofoam-CMU &Geofoam-Bridge slab	/	26.6	0
Bridge slab-Backfill soil	0.9	35.1	0
Bridge slab-Geotextile	/	16.2	9.5

changes to the interface friction angles δ based on the change of the friction angle of the backfill soil. Table 5 summarizes the interface properties used in the parametric study.

When the reinforcement spacing S_v was larger than 0.2 m, two CMU facing blocks were frictionally connected with each other without a geotextile layer in between. In other words, the interfaces between CMU facing blocks needed to be considered. Based on the recommendation by ACI [8], a friction coefficient of 0.6 was assigned to the interfaces between two CMU facing blocks in the parametric study. Consequently, the interface friction angle between two CMU facing blocks δ was equal to arctan(0.6) = 31.0°.

Similar modeling procedure was used in the parametric study as that used in the Virginia GRS-IBS study except that compaction was not simulated in the parametric study. For the trapezoidal layout, the modeling procedure was identical to that described in Section 3.3. For the uniform layout, the same modeling procedure was used except that a different approach was adopted for Stage 2 since the uniform layout did not have a RSF at the bottom. Instead, a 0.7 m thick embedment existed in front of the abutment facing in the uniform layout. Therefore, the following steps were implemented for Stage 2 in the uniform layout: a layer of the CMU facing blocks, the backfill soil, the retained soil, the embedment soil in front of the abutment facing, and the geotextiles were installed until the abutment height reached 0.7 m. The corresponding interfaces and connections were then assigned.

4.2. Additional vertical stress induced by bridge slab loading

Vertical stress under the beam seat centerline is important for the design of the required reinforcement strength [4]. Vertical stresses were extracted from the numerical simulations at the end of Stages 4 and 5 under the beam seat centerline. The additional vertical stress in this paper refers to the vertical stress induced by the bridge slab load and was calculated as the difference of the vertical stresses between Stages 4 and 5. It should be noted that the location of interest (i.e., beam seat centerline) changed with the change of the beam seat width and the setback distance. Fig. 10 shows that the two reinforcement layouts resulted in similar profiles of the additional vertical stresses with depth. The additional vertical stresses induced by the bridge slab load were highest at the top of the abutment and decreased sharply with depth until a certain depth. At greater depths, the uniform layout resulted in almost constant additional vertical stresses with a small reduction with depth. The trapezoidal layout, however, resulted in higher additional vertical stresses at the bottom of the abutment. This difference could be due to the existence of the RSF in the trapezoidal layout as opposed to the embedment in front of the CMU facing blocks in the uniform layout. Fig. 10(a) shows that different combinations of the reinforcement spacing S_v and reinforcement stiffness J did not result in significant difference in the profiles of the additional vertical stresses when the ratio of J/S_v was kept the same. Fig. 10(b) shows that, as expected, larger beam seat width b resulted in lower additional vertical stresses induced by the bridge slab load under the beam seat centerline. The effect of the beam seat width was more significant at the top of the abutment and diminished with depth since the influence of the bridge slab load became limited at greater depths. Fig. 10(c) shows that lower additional vertical stresses under the beam seat centerline were induced by the bridge slab load when a larger setback distance a_b was used. The use of a large setback distance a_b could prevent soil from yielding close to the abutment facing, thus reducing the additional vertical stress induced by the bridge slab load.

Fig. 10 also shows the calculated additional vertical stresses using both the Boussinesq solution recommended by the FHWA for the GRS-IBS [4] and the truncated 2 to 1 distribution recommended by both the FHWA for MSE walls [11] and the AASHTO [1]. The Boussinesq solution estimates the additional vertical stress induced by the bridge slab load $\Delta\sigma_v$ as follows:

$$\Delta\sigma_v = \frac{q}{\pi}[\alpha + \sin\alpha\cos(\alpha + 2\beta)] \tag{1}$$

$$q = \frac{0.5\rho_b g L_b D}{b} \tag{2}$$

where q is the surcharge pressure caused by the bridge slab load; α and β are two inclination angles for the point of interest; ρ_b is the density of the bridge slab (ρ_b = 2500 kg/m^3); L_b is the length of the bridge slab, (L_b = 15 m); D is the thickness of the bridge slab (D = 0.4 m); and b is the beam seat width (b of 0.6, 0.9, and 1.2 m were used in the parametric study).

When the point of interest was located under the beam seat centerline, the two inclination angles α and β can be calculated using Eqs. (3) and (4) as follows:

$$\alpha = \arctan\left(\frac{b/2}{z}\right) - \beta \tag{3}$$

$$\beta = \arctan\left(\frac{-b/2}{z}\right) \tag{4}$$

where z is the depth from the top of the abutment.

The truncated 2 to 1 distribution differs from the Boussinesq distribution by considering the existence of the abutment facing on the stress distribution as shown in Eqs. (5) to (9):

$$\Delta\sigma_v = \frac{Q}{D_1} \tag{5}$$

$$D_1 = b + z,\ z \leqslant z_1 \tag{6}$$

$$D_1 = \frac{b + z}{2} + d,\ z > z_1 \tag{7}$$

$$d = \frac{b}{2} + a_b \tag{8}$$

$$z_1 = 2d - b = 2a_b \tag{9}$$

where Q is the load per meter induced by the bridge slab self-weight ($Q = 0.5\rho_b g L_b D$ = 73.5kN/m); D_1 is the effective width of the applied load at a given depth z; b is the beam seat width (b of 0.6, 0.9, and 1.2 m were used in the parametric study); d is the distance between the beam seat centerline to the back of the abutment facing; a_b is the setback distance (a_b of 0.2, 0.4, and 0.8 m were used in the parametric study); and z_1 is the depth where the effective width intersects the back of the abutment facing.

Fig. 10(a) and (b) show that the Boussinesq solution was able to accurately predict the profile of the additional vertical stress induced by the bridge slab load although some difference was observed at the top of the abutment. The truncated 2 to 1 distribution, on the other hand, yielded slightly lower additional vertical stresses than the Boussinesq distribution within the depth ranging between 0 to approximately 1.5b vertically below the load. At greater depths, the truncated 2 to 1 distribution overestimated the additional vertical stresses. Both the Boussinesq distribution and the truncated 2 to 1 distribution overestimated the additional vertical stresses at the top of the abutment.

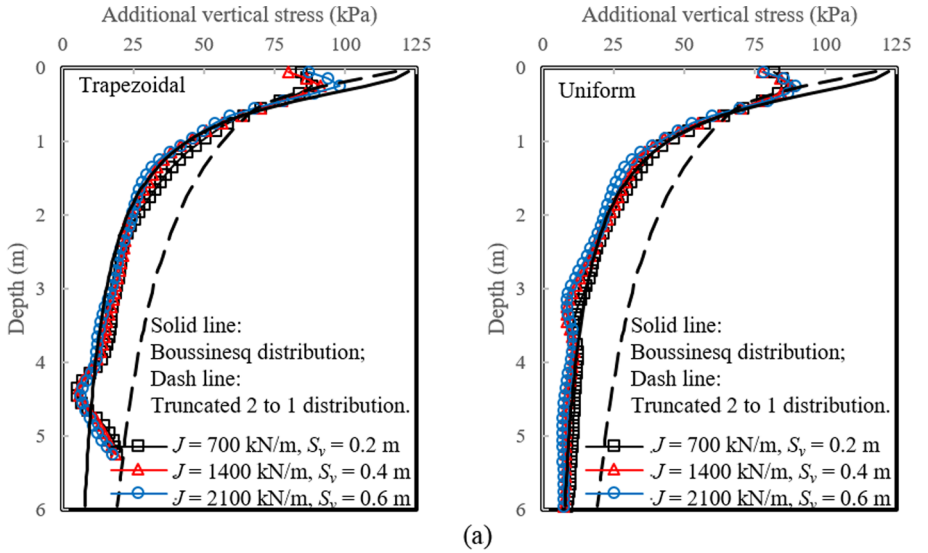

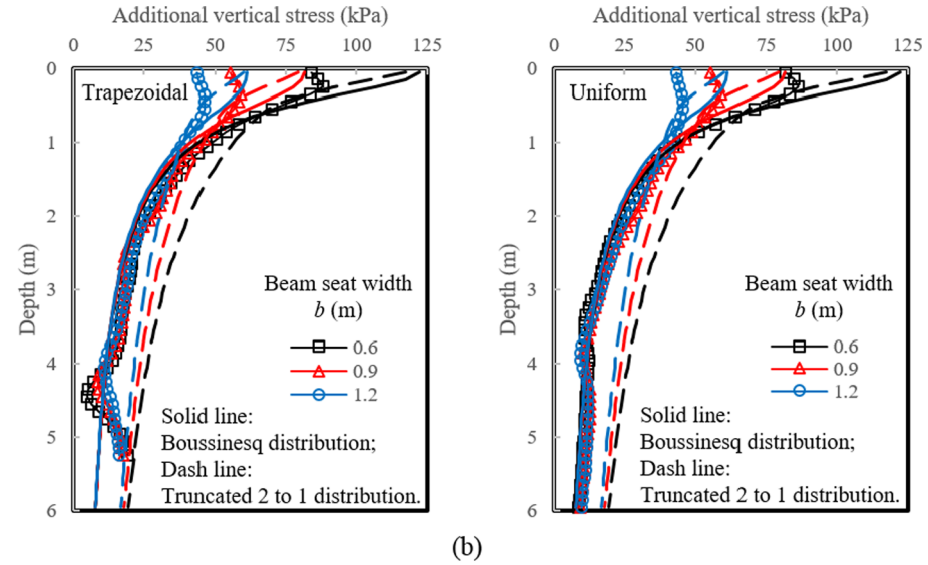

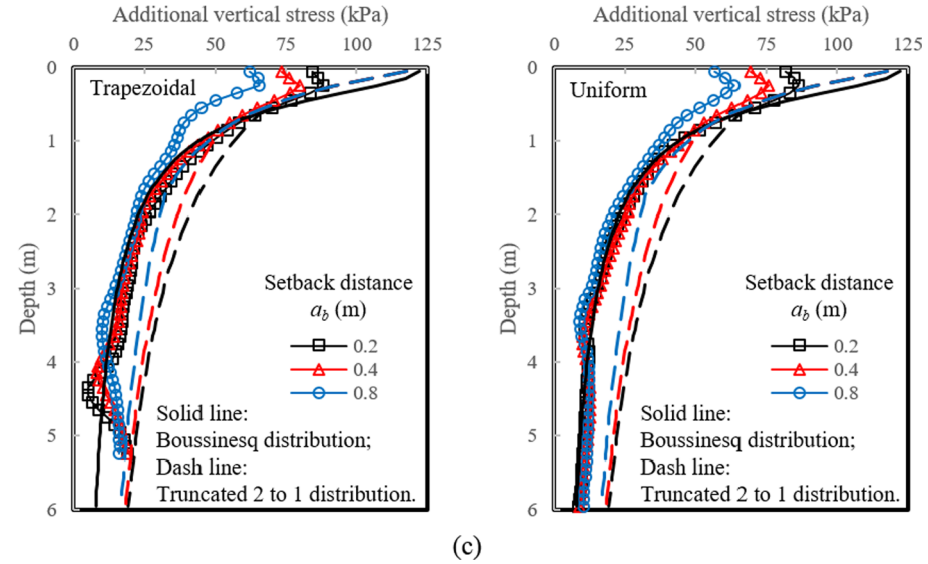

Fig. 10. Profiles of additional vertical stresses under the beam seat centerline induced by bridge slab loading: (a) effect of different combinations of reinforcement spacing S_v and reinforcement stiffness J with $b = 0.6$ m and $a_b = 0.2$ m; (b) effect of beam seat width b with $J = 700$ kN/m, $S_v = 0.2$ m, and $a_b = 0.2$ m; and (c) effect of setback distance a_b with $J = 700$ kN/m, $S_v = 0.2$ m, and $b = 0.6$ m.

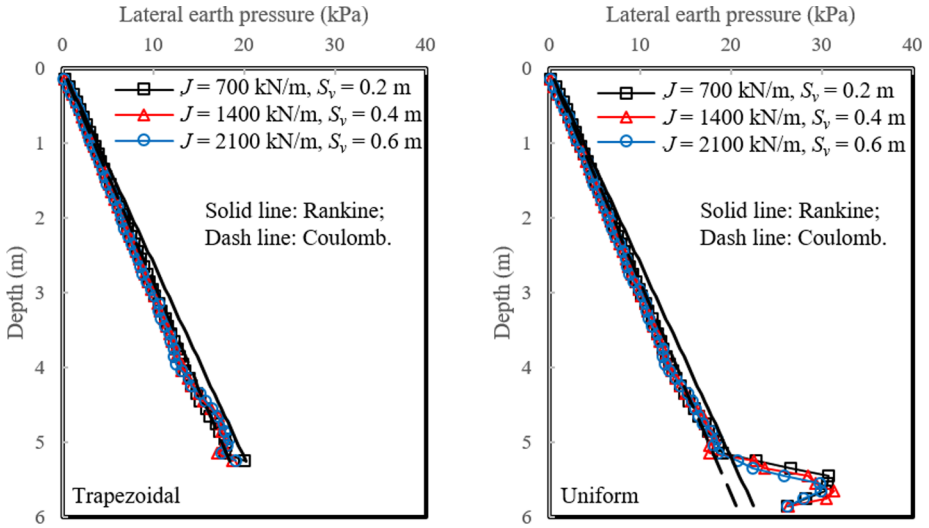

Fig. 11. Profiles of lateral earth pressures behind the abutment facing at the end of Stage 4 considering different combinations of reinforcement spacing S_v and reinforcement stiffness J with $b = 0.6$ m and $a_b = 0.2$ m.

The use of the geofoam in front of the beam seat reduced the additional vertical stresses at the top of the abutment. Fig. 10(c) shows that the Boussinesq distribution generated the same stress distributions despite the change of the setback distance a_b since the Boussinesq method did not consider the effects of the abutment facing on the stress distribution, which is not consistent with the numerical results. The truncated 2 to 1 distribution was able to predict lower additional vertical stresses at greater depths with an increase in the setback distance, which is more reasonable than the Boussinesq distribution.

4.3. Lateral earth pressure

Lateral earth pressure behind the abutment facing is crucial to define the required connection strengths of reinforcement layers. Fig. 11 shows the distributions of the lateral earth pressures behind the abutment facing at the end of Stage 4 considering different combinations of reinforcement spacing S_v and reinforcement stiffness J. Since these results were extracted from the numerical simulations at the end of Stage 4 prior to the placement of the bridge slab, they were not affected by different beam seat width b and setback distance a_b. Fig. 11 indicates that the results from both layouts were close to each other for the whole free abutment height of 5.3 m. For the uniform layout, the lateral earth pressure at the bottom of the abutment increased significantly, followed by a decrease. This change of the lateral earth pressure at the bottom of the abutment was due to the embedment in front of the CMU facing blocks. As noted previously in Section 4.1, the embedment was constructed along with the construction of the bottom layers of the GRS abutment, which is different from the common practice that the embedment is not added until the whole abutment is finished. Similar to the additional vertical stress, different combinations of the reinforcement spacing S_v and reinforcement stiffness J did not lead to significant difference in the lateral earth pressure profiles behind the abutment facing when the ratio of J/S_v was kept the same.

Fig. 11 also shows the theoretical distributions of active lateral earth pressures using both Rankine's and Coulomb's methods. The Rankine active earth pressure coefficient for the backfill soil with a friction angle of 38° is 0.24 and the Coulomb active earth pressure coefficient is 0.22 considering the friction between the abutment facing and the backfill soil. Fig. 11 shows that the numerical results are in good agreement with the Coulomb active earth pressure distribution. The Rankine active earth pressure distribution slightly overestimated the lateral earth pressure at greater depth where the effects of the friction between the abutment facing and the backfill soil became more pronounced with the increase of the overburden stress.

Fig. 12 presents the profiles of additional lateral earth pressures behind the abutment facing induced by the bridge slab load. Fig. 12 shows that the two reinforcement layouts resulted in similar profiles of the additional lateral earth pressures along depth. Both Fig. 12(a) and (b) show similar distribution shapes of the additional lateral earth pressures with the peak occurring at a certain depth below the load. Fig. 12(a) indicates that different combinations of the reinforcement spacing S_v and reinforcement stiffness J did not have a significant effect on the profiles of the additional lateral earth pressures behind the abutment facing when the ratio of J/S_v was kept the same. Fig. 12(b) and (c) show that, as expected, an increase of the beam seat width b and the setback distance a_b led to lower additional lateral earth pressures behind the abutment facing. Furthermore, Fig. 12(c) shows that an increase of a_b from 0.4 m to 0.8 m changed the distribution shape of the additional lateral earth pressures behind the abutment facing. When a setback distance a_b of 0.8 m was used, the location of the peak additional lateral earth pressure clearly moved downward.

Fig. 12 also shows the calculated additional lateral earth pressures behind the abutment facing using the Boussinesq solution with and without considering soil yielding. The Boussinesq solution recommended by the FHWA for the GRS-IBS [4] estimates the additional lateral earth pressure behind the abutment facing induced by the bridge slab load $\Delta\sigma_{h\text{-}facing}$ based on Eq. (10) as follows:

$$\Delta\sigma_{h\ -\ facing} = \frac{q}{\pi}[\alpha + \sin\alpha\cos(\alpha + 2\beta)]K_a \tag{10}$$

where q is the surcharge pressure caused by the bridge slab load and can be calculated using Eq. (2); α and β are two inclination angles for the point of interest; and K_a is the Rankine active earth pressure coefficient for the backfill soil ($K_a = 0.24$).

When calculating the additional lateral earth pressure behind the abutment facing, the point of interest changed from the beam seat centerline to the abutment facing. Therefore, the two inclination angles α and β can be calculated using Eqs. (11) and (12) as follows:

$$\alpha = \arctan\left(\frac{b + a_b}{z}\right) - \beta \tag{11}$$

$$\beta = \arctan\left(\frac{a_b}{z}\right) \tag{12}$$

The calculated profiles of the additional lateral earth pressures using Eq. (10) are shown in Fig. 12 using the solid lines. Clearly, Eq. (10) underestimated the additional lateral earth pressures. Therefore, the

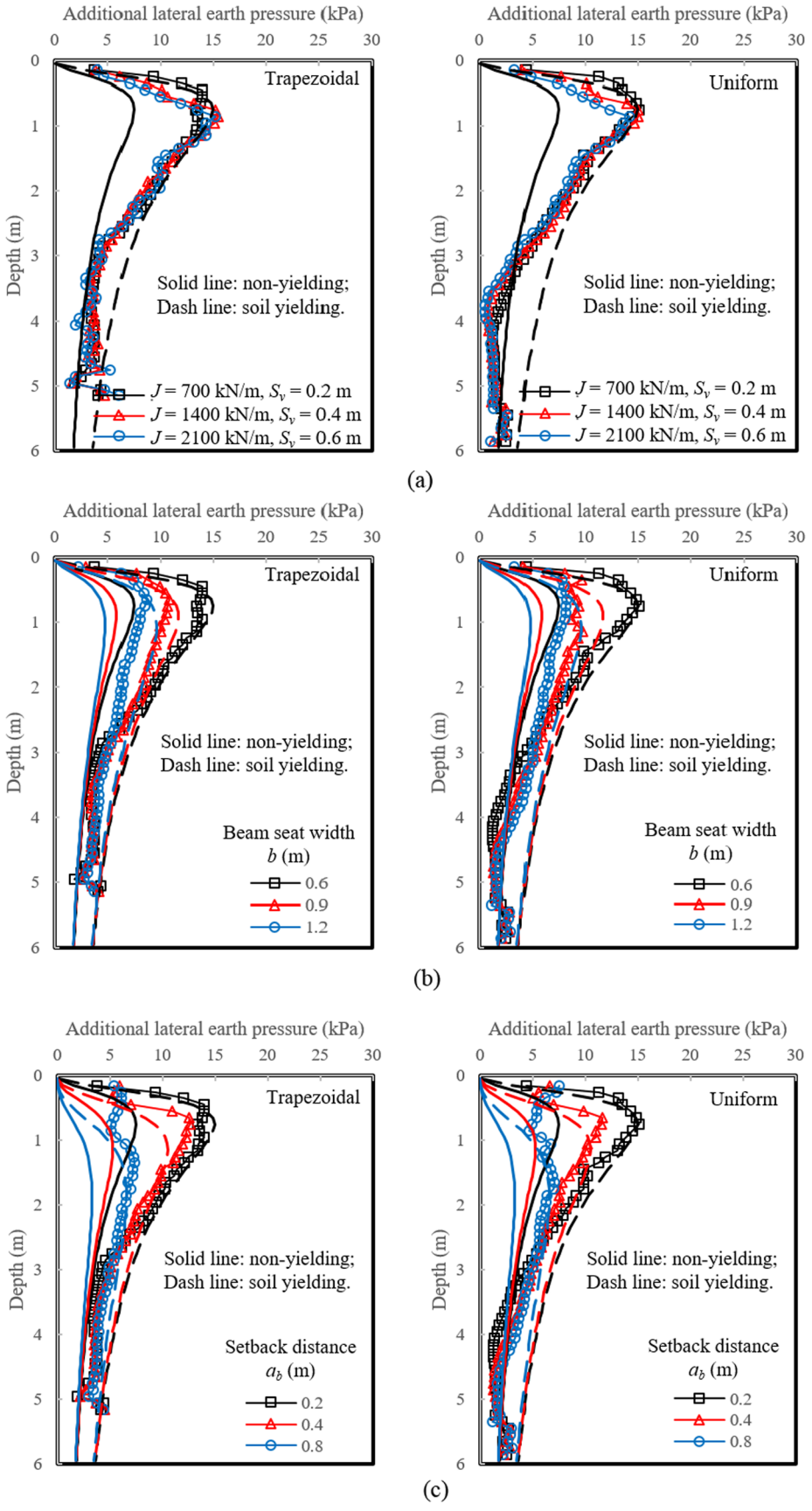

Fig. 12. Profiles of additional lateral earth pressures behind the abutment facing induced by bridge slab loading: (a) effect of different combinations of reinforcement spacing S_v and reinforcement stiffness J with b = 0.6 m and a_b = 0.2 m; (b) effect of beam seat width b with J = 700 kN/m, S_v = 0.2 m, and a_b = 0.2 m; and (c) effect of setback distance a_b with J = 700 kN/m, S_v = 0.2 m, and b = 0.6 m.

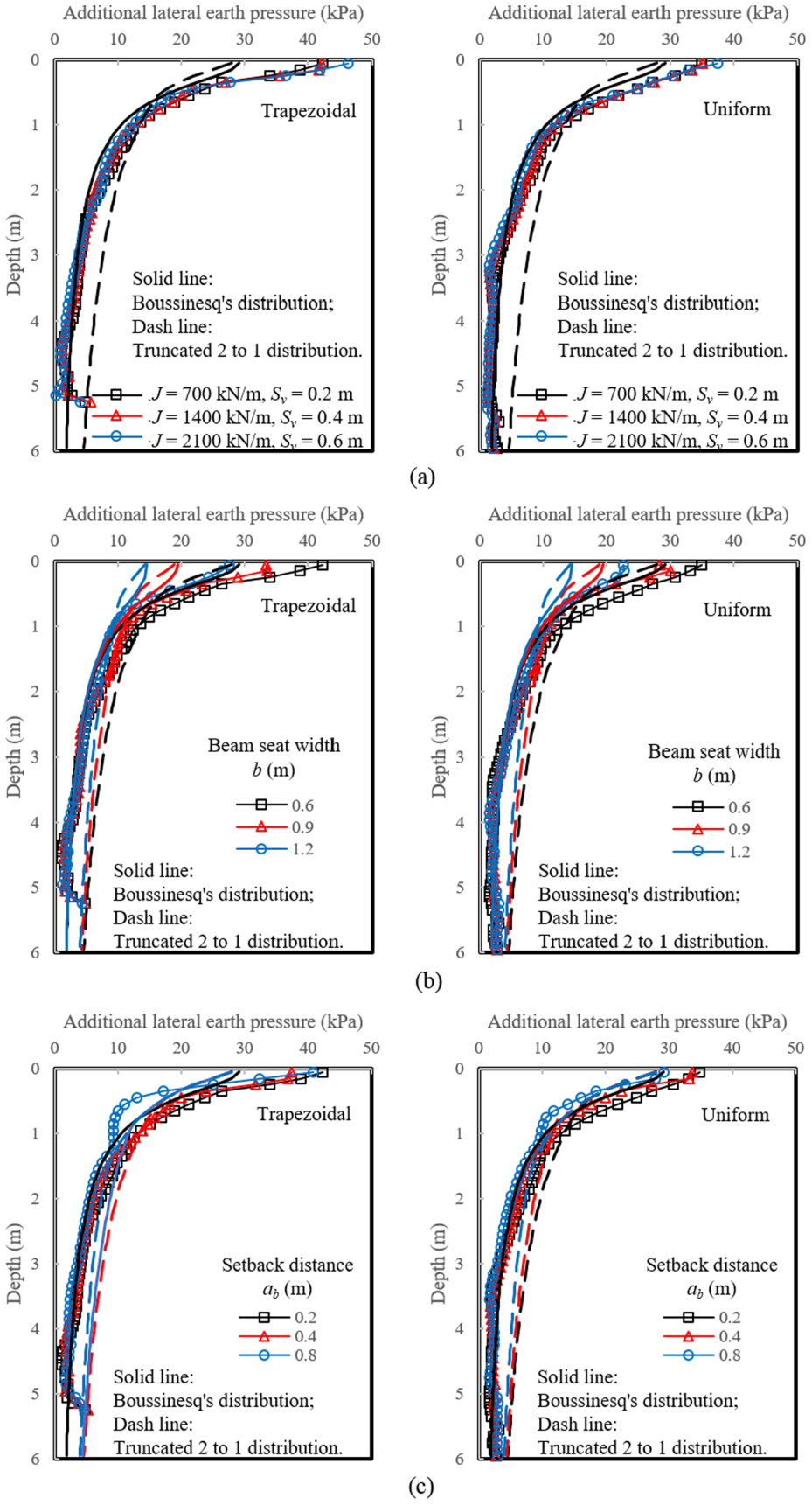

Fig. 13. Profiles of additional lateral earth pressures under the beam seat centerline induced by bridge slab loading: (a) effect of different combinations of reinforcement spacing S_v and reinforcement stiffness J with $b = 0.6$ m and $a_b = 0.2$ m; (b) effect of beam seat width b with $J = 700$ kN/m, $S_v = 0.2$ m, and $a_b = 0.2$ m; and (c) effect of setback distance a_b with $J = 700$ kN/m, $S_v = 0.2$ m, and $b = 0.6$ m.

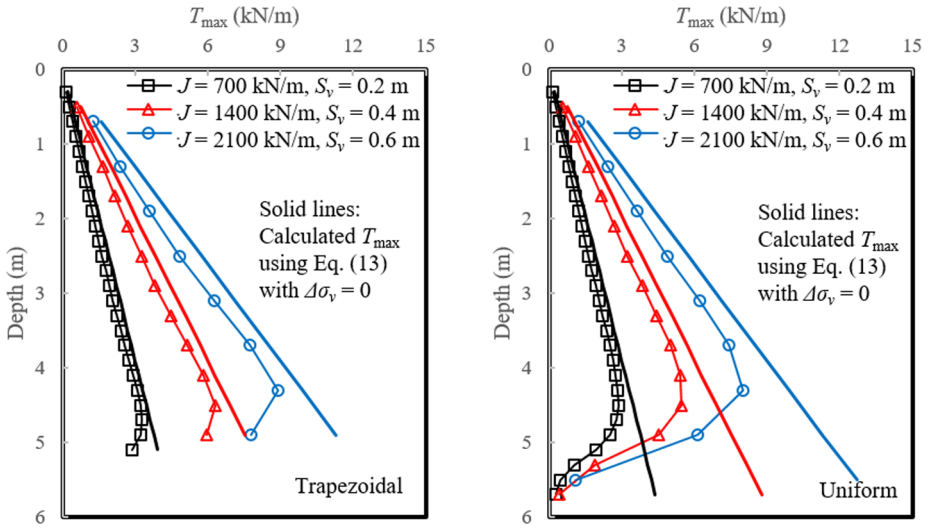

Fig. 14. Distributions of maximum tension in the reinforcement T_{max} at the end of Stage 4 considering different combinations of reinforcement spacing S_v and reinforcement stiffness J with b = 0.6 m and a_b = 0.2 m.

right-hand side of Eq. (10) is doubled to account for the soil yielding at the abutment facing [14] and the calculated results considering the soil yielding effect are shown in Fig. 12 using the dash lines. Fig. 12 shows that the calculated distributions considering soil yielding matched reasonably well with the numerical results in terms of both the magnitudes and the distribution shapes of the additional lateral earth pressures behind the abutment facing induced by the bridge slab load.

Apart from the lateral earth pressures behind the abutment facing, the lateral earth pressures under the beam seat are also important to the design of the GRS abutments since the beam seat centerline is the critical location for the maximum reinforcement tension [4]. Zheng et al. [39] also reported that the maximum strain in the reinforcement occurred under the beam seat centerline in upper reinforcement layers. Fig. 13 presents the profiles of additional lateral earth pressures under the beam seat centerline induced by the bridge slab load. The two reinforcement layouts resulted in similar profiles of the additional lateral earth pressures along depth except that the trapezoidal layout predicted slightly higher additional lateral earth pressures near the top of the abutment. The effects of different combinations of S_v and J and the effects of b on the profiles of the additional lateral earth pressures under the beam seat centerline were similar to those behind the abutment facing. Fig. 13 also shows the calculated additional lateral earth pressures under the beam seat centerline induced by the bridge slab load $\Delta\sigma_{h\text{-}center}$ using the Boussinesq solution and the truncated 2 to 1 distribution. Both the Boussinesq solution and the truncated 2 to 1 distribution estimate the $\Delta\sigma_{h\text{-}center}$ based on the product of the Rankine active earth pressure coefficient for the backfill soil K_a and the additional vertical stress under the beam seat centerline $\Delta\sigma_v$ (i.e., $\Delta\sigma_{h\text{-}center} = K_a \cdot \Delta\sigma_v$). Equations (1) to (4) were used in the Boussinesq solution to calculate the $\Delta\sigma_v$ while Eq. (5) to (9) were used in the truncated 2 to 1 distribution to calculate the $\Delta\sigma_v$. Fig. 13 shows that both methods underestimated the additional lateral earth pressures under the beam seat centerline at the top portion of the GRS abutments regardless the change of beam seat width b, setback distance a_b, and different combinations of reinforcement spacing S_v and reinforcement stiffness J. At greater depths, the truncated 2 to 1 distribution overestimated the additional lateral earth pressures while the Boussinesq solution accurately predict the additional lateral earth pressures. Similar to the distribution of the additional vertical stresses induced by the bridge slab load, Fig. 13(c) shows that the Boussinesq distribution did not reflect the effect of setback distance a_b on the distribution of the additional lateral earth pressures, which is neither reasonable nor consistent with the numerical results.

4.4. Tension in reinforcement layers

Fig. 14 shows the distribution of the maximum tension in the reinforcement T_{max} at the end of Stage 4 considering different combinations of reinforcement spacing S_v and reinforcement stiffness J. Since these results were extracted from the numerical simulations at the end of Stage 4 prior to the placement of the bridge slab, they were not affected by different beam seat widths b and setback distances a_b. For the trapezoidal layout, the maximum T_{max} with depth were 3.3, 6.3, and 8.9 kN/m for the cases with S_v of 0.2, 0.4, and 0.6 m respectively. For the uniform layout, the maximum T_{max} with depth were 2.9, 5.4, and 8.0 kN/m for the cases with S_v of 0.2, 0.4, and 0.6 m respectively. Therefore, the maximum tension in the reinforcement decreased almost proportionally with the decrease of reinforcement spacing S_v. Fig. 14 also shows the calculated T_{max} profile with depth using Eq. (13) recommended by AASHTO with $\Delta\sigma_v$ being zero. Fig. 14 shows that the calculated T_{max} profile using Eq. (13) matched reasonably well with the numerical results except for the bottom portion of the abutment. The RSF in the trapezoidal layout and the embedment soil in front of the CMU facing blocks in the uniform layout acted as toe resistance, thus resulting in lower T_{max} in the bottom portion of the abutment. However, Eq. (13) did not consider these effects and therefore overestimated the T_{max} values in the bottom reinforcement layers:

$$T_{max} = K_a(\rho g z + \Delta\sigma_v)S_v \quad (13)$$

where K_a is the Rankine active earth pressure coefficient for the backfill soil (K_a = 0.24); ρ is the density of the backfill soil (ρ = 1650 kg/m^3); z is the depth from the top of the abutment; $\Delta\sigma_v$ is the additional vertical stress induced by the bridge slab load and could be calculated using Eq. (1) or (5); and S_v is the reinforcement spacing (S_v of 0.2, 0.4, and 0.6 m were used in the parametric study).

Fig. 15 shows the distributions of the maximum tension in the reinforcement T_{max} at the end of Stage 5 (i.e., after the placement of the bridge slab). Both the trapezoidal and the uniform layouts yielded similar distributions of T_{max} in the reinforcement. As compared with Fig. 14, Fig. 15 shows that T_{max} in the upper reinforcement layers increased significantly due to bridge slab loading while the change of T_{max} in the bottom reinforcement layers was relatively smaller. Fig. 15(a) shows the effects of different combinations of reinforcement spacing S_v and reinforcement stiffness J on the T_{max} distribution. For the trapezoidal layout, the maximum T_{max} with depth were 4.5, 8.4, and 11.5 kN/m for the cases with S_v of 0.2, 0.4, and 0.6 m respectively. For the uniform layout, the maximum T_{max} with depth were 3.4, 6.4, and

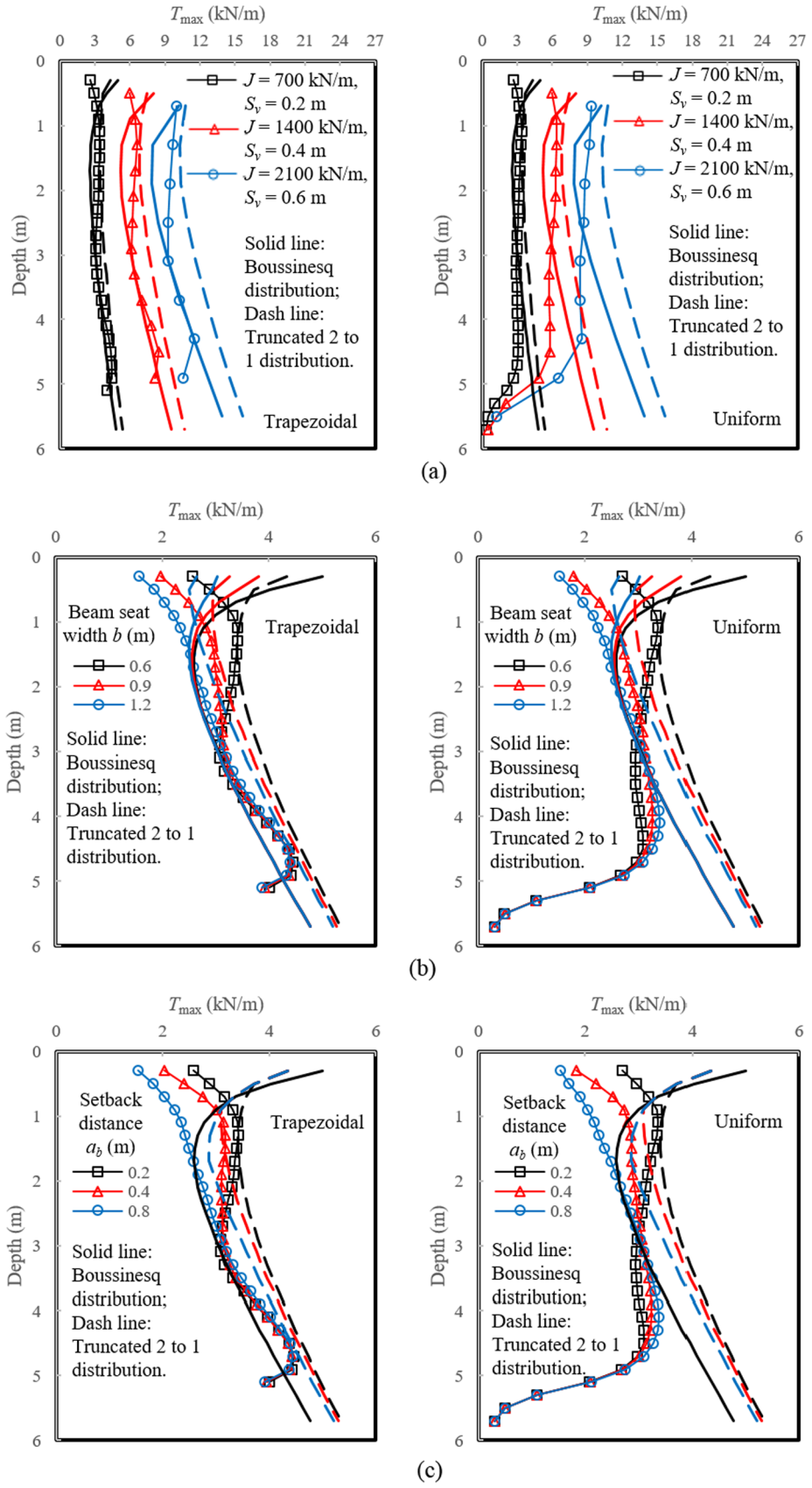

Fig. 15. Distributions of maximum tension in the reinforcement T_{max} at the end of Stage 5: (a) effect of different combinations of reinforcement spacing S_v and reinforcement stiffness J with b = 0.6 m and a_b = 0.2 m; (b) effect of beam seat width b with J = 700 kN/m, S_v = 0.2 m, and a_b = 0.2 m; and (c) effect of setback distance a_b with J = 700 kN/m, S_v = 0.2 m, and b = 0.6 m.

9.1 kN/m for the cases with S_v of 0.2, 0.4, and 0.6 m respectively. Therefore, the maximum tension in the reinforcement decreased almost proportionally with the decrease of reinforcement spacing S_v without any bridge slab load (i.e., at the end of Stage 4 as previously shown in Fig. 14) and with a bridge slab load (i.e., at the end of Stage 5) when the ratio of J/S_v was kept the same. Fig. 15(b) and (c) show that, as expected, the increase of the beam seat width b and the setback distance a_b resulted in smaller T_{max} in the upper reinforcement layers. Limited effect was found for b and a_b on the T_{max} in the bottom reinforcement layers since the bottom of the abutment was too far away from the top loading area.

Fig. 15 also presents the calculated T_{max} profiles with depth using Eq. (13) recommended by AASHTO with $\Delta\sigma_v$ calculated using both the Boussinesq solution (Eq. (1)) and the truncated 2 to 1 distribution (Eq. (5)). Fig. 15 shows that the Boussinesq solution underestimated the T_{max} values in the reinforcement layers at the middle to upper portion of the abutment, which is not conservative in design. The truncated 2 to 1 distribution method, on the other hand, slightly overestimated the distribution of T_{max} in the reinforcement layers, which is more conservative. Similar to the distribution of the additional vertical stresses induced by the bridge slab load, Fig. 15(c) shows that the Boussinesq distribution did not reflect the effect of setback distance a_b on the distribution of T_{max} in the reinforcement layers, which is neither reasonable nor consistent with the numerical results.

5. Conclusions

The objective of this study was to evaluate the responses of geosynthetic-reinforced soil (GRS) abutments subjected to bridge slab loading under working stress conditions using the two-dimensional finite difference numerical method. The results of the numerical model developed in this study were compared to the field data of a monitored geosynthetic reinforced soil – integrated bridge system (GRS-IBS) in Virginia, USA to verify its ability to predict the abutment behavior under bridge slab loading. A parametric study was then conducted to investigate the effects of the following influencing factors, including different combinations of reinforcement spacing S_v and reinforcement stiffness J, beam seat width b, and setback distance a_b, on the responses of the GRS abutments in terms of the additional vertical stresses and the lateral earth pressures induced by the bridge slab load and the maximum tension T_{max} in the reinforcement. Two different reinforcement layouts, trapezoidal and uniform, were evaluated in the parametric study. The following conclusions can be drawn from this study:

(1) Both reinforcement layouts resulted in similar responses of the GRS abutment with and without bridge slab loading. The embedment in front of the abutment facing blocks formed during the construction of the lower abutment layers led to smaller T_{max} in the bottom reinforcement layers in the uniform layout as compared to those in the trapezoidal layout.
(2) Different combinations of the reinforcement spacing S_v and reinforcement stiffness J did not result in significant difference in the profiles of the additional vertical stresses under the beam seat centerline and the additional lateral earth pressures behind the abutment facing induced by the bridge slab load when the ratio of J/S_v was kept the same. The maximum of T_{max} in the reinforcement with depth decreased almost proportionally with the decrease of the reinforcement spacing S_v with and without a bridge slab load when the ratio of J/S_v was kept the same.
(3) Larger beam seat width b and setback distance a_b resulted in lower additional vertical stresses under the beam seat centerline and lower additional lateral earth pressures behind the abutment facing induced by the bridge slab load. The increase of the beam seat width b and the setback distance a_b resulted in smaller T_{max} in the upper reinforcement layers. Limited effect was found for b and a_b on the T_{max} in the bottom reinforcement layers
(4) Both the Boussinesq solution method and the truncated 2 to 1 distribution method were able to reasonably predict the profiles of the additional vertical stresses under the beam seat centerline induced by the bridge slab load. However, both methods underestimated the additional lateral earth pressures under the beam seat centerline at the top portion of the GRS abutments. The Boussinesq method did not consider the effect of the abutment facing on the stress distribution, which is not consistent with the numerical results.
(5) The Boussinesq distribution method underestimated the additional lateral earth pressures behind the abutment facing induced by the bridge slab load. The Boussinesq distribution method considering soil yielding could reasonably capture both the magnitudes and the distribution shapes of the additional lateral earth pressures behind the abutment facing induced by the bridge slab load.
(6) The Boussinesq distribution method underestimated the maximum tension T_{max} in the reinforcement layers within the middle to upper portion of the abutment. The truncated 2 to 1 distribution method, on the other hand, slightly overestimated the distribution of T_{max} in the reinforcement layers, which is more conservative in design.

It should be noted that the numerical analyses conducted in this study simulated the responses of the GRS abutments under working stress conditions, which may be different from the behavior of the GRS abutments under strength limit conditions.

CRediT authorship contribution statement

Panpan Shen: Methodology, Software, Investigation, Writing - original draft. **Jie Han:** Conceptualization, Investigation, Writing - review & editing, Supervision. **Jorge G. Zornberg:** Supervision, Conceptualization, Writing - review & editing. **Burak F. Tanyu:** Validation, Writing - review & editing. **Barry R. Christopher:** Investigation, Writing - review & editing. **Dov Leshchinsky:** Investigation, Writing - review & editing.

Declaration of Competing Interest

The authors declare that they have no known competing financial interests or personal relationships that could have appeared to influence the work reported in this paper.

Acknowledgements

This research was supported by the National Cooperative Highway Research Program (NCHRP) under Project 24-41. The opinions presented in this paper are exclusively those of the authors and not necessarily those of the NCHRP. The authors would like to acknowledge this support.

References

[1] AASHTO. LRFD Bridge Design Specifications. 8th ed. Washington, DC: AASHTO; 2017.
[2] Abu-Hejleh N, Zornberg JG, Wang T, Watcharamonthein J. Monitored displacements of unique geosynthetic-reinforced soil bridge abutments. Geosynthetics International 2002;9(1):71–95.
[3] Adams, M. T., Ketchart, K., & Wu, J. T. H., 2007. Mini Pier Experiments: Geosynthetic Reinforcement Spacing and Strength as Related to Performance. Geosynthetics in Reinforcement and Hydraulic Applications. Geotechnical Special Publication 165, Geo-Denver, Reston, VA.
[4] Adams, M., & Nicks, J., 2018. Design and Construction Guidelines for Geosynthetic Reinforced Soil Abutments and Integrated Bridge Systems. FHWA-HRT-17-080.
[5] Ahmadi H, Bezuijen A. Full-scale mechanically stabilized earth (MSE) walls under strip footing load. Geotext Geomembr 2018;46(3):297–311.
[6] Allen TM, Bathurst RJ, Holtz RD, Walters DL, Lee WF. A new working stress method for prediction of reinforcement loads in geosynthetic walls. Can Geotech J 2003;40:976–94.
[7] Ambauen S, Leshchinsky B, Xie Y, Rayamajhi D. Service-state behavior of reinforced soil walls supporting spread footings: a parametric study using finite-element analysis. Geosynthetics International 2016;23(3):156–70.

[8] American Concrete Institute (ACI). Building Code Requirements for Structural Concrete (ACI 318–02) and Commentary (ACI 318R–02). MI: Farmington Hills; 2002.
[9] Awad MI, Tanyu BF. Laboratory evaluation of governing mechanism of frictionally connected MSEW face and implications on design. Geotext Geomembr 2014;42:468–78.
[10] Bathurst RJ, Allen TM, Walters DL. Reinforcement loads in geosynthetic walls and the case for a new working stress design method. Geotext Geomembr 2005;23(4):287–322.
[11] Berg, R. R., Christopher, B. R., & Samtani, N., 2009. Mechanically Stabilized Earth Walls and Reinforced Soil Slopes, Design and Construction Guidelines. U.S. Department of Transportation, Federal Highway Administration, Washington DC, FHWA-NHI-09-083 and FHWA GEC011, 668p.
[12] Bolton M. The strength and dilatancy of sands. Geotechnique 1986;36:65–78.
[13] Coduto DP. Foundation design: principles and practices. Pearson; 2015.
[14] Das Braja M. Principles of Foundation Engineering. (7th Ed.). Cengage Learning; 2011.
[15] Elton D, Patawaran MA. Mechanically stabilized earth reinforcement tensile strength from tests of geotextile-reinforced soil. Transportation Research Record: Journal of the Transportation Research Board 2004;1868:81–8.
[16] Gebremariam F, Tanyu BF, Christopher B, Leshchinsky D, Han J, Zornberg JG. Evaluation of vertical stress distribution in field monitored GRS-IBS structure. Geosynthetics International 2020. https://doi.org/10.1680/jgein.20.00004 (in press).
[17] Han J, Leshchinsky D. General analytical framework for design of flexible reinforced earth structures. J Geotech Geoenviron Eng 2006;132(11):1427–35.
[18] Hatami K, Bathurst RJ. Development and verification of a numerical model for the analysis of geosynthetic-reinforced soil segmental walls under working stress conditions. Can Geotech J 2005;42:1066–85.
[19] Helwany SMB, Wu JTH, Kitsabunnarat A. Simulating the behavior of GRS bridge abutments. J Geotech Geoenviron Eng 2007;133(10):1229–40.
[20] Huang B, Bathurst RJ, Hatami K. Numerical study of reinforced soil segmental walls using three different constitutive soil models. J Geotech Geoenviron Eng 2009;135:1486–98.
[21] Itasca Consulting Group. FLAC Theory and Background. Itsca Consulting. Group Inc.; 2008.
[22] Leshchinsky D, Kang B, Han J, Ling H. Framework for limit state design of geosynthetic-reinforced walls and slopes. Transportation Infrastructure Geotechnology 2014;1(2):129–64.
[23] Leshchinsky D, Leshchinsky B, Leshchinsky O. Limit state design framework for geosynthetic-reinforced soil structures. Geotext Geomembr 2017;45(6):642–52.
[24] Mitchell JK, Soga K. Fundamentals of soil behavior. John Wiley & Sons Inc; 2005.
[25] Negussey D. Design parameters for EPS geofoam. Soils Found 2007;47:161–70.
[26] Nicks, J. E., Adams, M., Ooi, P., & Stabile, T., 2013. Geosynthetic reinforced soil performance testing - Axial load deformation relationships. FHWA-HRT-13-066.
[27] Pham, T.Q., 2009. Investigating Composite Behavior of Geosynthetic Reinforced Soil (GRS) Mass. Ph. D. Thesis. University of Colorado, Denver, USA.
[28] Saghebfar M, Abu-Farsakh M, Ardah A, Chen Q, Fernandez BA. Performance monitoring of Geosynthetic Reinforced Soil Integrated Bridge System (GRS-IBS) in Louisiana. Geotext Geomembr 2017;45(2):34–47.
[29] Wu J, Ketchart K, Adams M. Two full-scale loading experiments of geosynthetic-reinforced soil (GRS) abutment wall. Int J Geotech Eng 2008;2(4):305–17.
[30] Xiao C, Han J, Zhang Z. Experimental study on performance of geosynthetic-reinforced soil model walls on rigid foundations subjected to static footing loading. Geotext Geomembr 2016;44(1):81–94.
[31] Xiao, M., Qiu, T., Khosrojerdi, M., Basu, P., & Withiam, J., 2016b. Synthesis and Evaluation of the Service Limit State of Engineered Fills for Bridge Support. FHWA-HRT-15-080.
[32] Xie Y, Leshchinsky B, Han J. Evaluation of Bearing Capacity on Geosynthetic-Reinforced Soil Structures Considering Multiple Failure Mechanisms. J Geotech Geoenviron Eng 2019;145(9):04019040.
[33] Xie Y, Leshchinsky B, Yang S. Evaluating reinforcement loading within surcharged segmental block reinforced soil walls using a limit state framework. Geotext Geomembr 2016;44(6):832–44.
[34] Xu C, Liang C, Shen P. Experimental and theoretical studies on the ultimate bearing capacity of geogrid-reinforced sand. Geotext Geomembr 2019;47(3):417–28.
[35] Zheng Y, Fox PJ. Numerical investigation of geosynthetic-reinforced soil bridge abutments under static loading. J Geotech Geoenviron Eng 2016;142(5):04016004.
[36] Zheng Y, Fox PJ. Numerical Investigation of the Geosynthetic Reinforced Soil-Integrated Bridge System under Static Loading. J Geotech Geoenviron Eng 2017;143(6):04017008.
[37] Zheng Y, Fox PJ, McCartney JS. Numerical simulation of deformation and failure behavior of geosynthetic reinforced soil bridge abutments. J Geotech Geoenviron Eng 2018;144(7):04018037.
[38] Zheng Y, Fox PJ, McCartney JS. Numerical study on maximum reinforcement tensile forces in geosynthetic reinforced soil bridge abutments. Geotext Geomembr 2018;46(5):634–45.
[39] Zheng Y, Fox PJ, Shing PB, McCartney JS. Physical model tests of half-scale geosynthetic reinforced soil bridge abutments. I: Static loading. J Geotech Geoenviron Eng 2019;145(11):04019094.
[40] Zornberg JG, Christopher BR, Leshchinsky D, Han J, Tanyu BF, Morsy AM, et al. Defining the boundary conditions for composite behavior of geosynthetic reinforced soil (GRS) structures. National Cooperative Highway Research Program (NCHRP), Project 24–41, Transportation Research Board, Washington 2019;DC:997p.